Production of Mg thin flakes with enhanced hydrogen storage performance

Joan S. Cortinez [a,*], Alejandro Gómez [b], Alejandro A. Zuleta Gil [c], José A. Tamayo [d], Esteban Correa [e], Francisco J. Bolívar [a], Félix Echeverria Echeverria [a]

[a] *Centro de Investigación, Innovación y Desarrollo de Materiales – CIDEMAT, Facultad de Ingeniería, Universidad de Antioquia UdeA, Calle 70 No 52 – 21, Medellín, Colombia*
[b] *Grupo Catalizadores y Adsorbentes – CATALAD, Instituto de Química, Universidad de Antioquia UdeA, Calle 70 No 52 – 21, Medellín, Colombia*
[c] *Grupo de Investigación de Estudios en Diseño - GED, Facultad de Diseño Industrial, Universidad Pontificia Bolivariana, Sede Medellín, Circular 1 No 70 – 01, Medellín, Colombia*
[d] *Grupo Calidad Metrología y Producción, Instituto Tecnológico Metropolitano ITM, Medellín, Antioquia, 050034, Colombia*
[e] *Grupo de Investigación Materiales con Impacto – MAT&MPAC, Facultad de Ingenierías, Universidad de Medellín UdeM, Carrera 87 No 30 – 65, Medellín, Colombia*

ARTICLE INFO

ABSTRACT

Flake-like particles are interesting materials for the preparation of alloys and homogeneous nanocomposites, they also have potential use as hydrogen storage materials. However, limited information is available regarding the synthesis of pure magnesium with flake-like morphology. In this study, the successful production of Mg flakes was conducted using a cost-effective and simple method, such as high energy ball milling. Various milling parameters, including different milling times and process control agents, were tested. Optimal conditions led to the formation of coarse flakes with ~1.72 μm thickness, while a two-step milling process produced thinner flakes with submicron thickness (~242 nm). Ductilization of the material and a significant reduction in crystal size during the milling process were observed via X-ray diffraction. Isothermal kinetic tests at 350 °C and 20 bar revealed improved hydrogen storage performance for both coarse and thin flakes compared to pristine Mg. Coarse flakes achieved capacities of 4.1 wt% in 60 min while thin flakes reached 4.6 wt% in 6 min, compared to 3.4 wt% achieved in 100 min by pristine Mg. The improved behavior of thin flake-shaped Mg was maintained at 300 °C and 20 bar, with 4.5 wt% of hydrogen absorbed in 6 min. Even at lower testing pressures (10 bar) higher capacities were achieved at the expense of slower kinetics. These findings suggest that thin flake-shaped Mg is a suitable material with enhanced performance for hydrogen storage applications.

1. Introduction

Interest in magnesium-based materials has been rising in the last decades due to its abundance on earth's crust, low density, low cost, high specific properties and its potential as a solid-state hydrogen storage material [1–8]. Among the many methods for processing Mg, High Energy Ball Milling (HEBM) has got great attention lately due to the possibility to prepare ultrafine materials with a wide range of properties at lower costs than conventional and complex synthesis methods [9,10] it is also an easily scalable process and is widely used for mechanical alloying of powders [11–17]. However, it is a complex process due to the high number of parameters involved in it, all of them influence on the shape and size modification of the material as a result of a transference of energy from the milling balls to the particles [18–20]. This energy could cause many phenomena, from comminution and grain refinement to ductilization of hcp materials and severe deformation of the particles [11].

This type of deformation could lead to flake-shaped particles, which are of special interest as precursors for the preparation of various alloys and nanocomposites due to their ability to promote the uniform distribution of additives in processes such as mechanical alloying [21,22]. Several applications have been reported for the use of flake-like shaped particles in this type of processes [23–28]. However, there is a lack of information about the production of flake-shaped powders of magnesium, which have potential for applications in the automotive, biomedical, aeronautical, and energetic fields [29]. In the latter, magnesium stands out as a promising solid-state storage material due to its ability to reversibly absorb and release hydrogen and its high gravimetric capacity (7.6 wt%) [15]. Nevertheless, it poorly performs in hydrogenation/dehydrogenation reactions, due to its slackened kinetics

and high thermodynamic stability, requiring morphological, microstructural and/or compositional modifications to promote faster sorption/desorption rates and lower pressure and temperature conditions for these processes to occur [11,30–37]. The aim of the present work is to assess the impact of various milling conditions, including milling time and the use of two process control agents (PCA), on the production of flake-like magnesium through high energy ball milling, conducted either in one or two stages. Additionally, kinetic performance in hydrogen sorption/desorption of the synthesized materials will be evaluated for its potential use as a solid-state storage material.

2. Experimental

2.1. Mg flakes preparation

Two types of Mg flakes were prepared from powders of commercially pure magnesium (96 wt%) from Tangshan Weihao Magnesium Powder Co. Milling took place in a Retsch Emax high-energy ball mill using stainless-steel jars with a ZrO_2 coating. All samples were handled in an argon-filled glovebox (Vigor Tech USA) with oxygen and moisture contents lower than 1 ppm. For the first set of flakes (which later will be referred as coarse flakes), milling speed of 300 rpm, filling vial percentage of 50% and ball-to-powder weight ratio (BPR) of 40:1 were kept constant, while zirconia ball size, milling/resting interval, milling time, hexane and stearic acid (SA) as process control agents (PCA) were varied in order to improve the flake content in the samples until obtaining the optimal quantity of flakes with desired morphology. Detailed conditions used for milling of coarse flakes can be found on Table 1.

To compare hydrogen storage performance of flakes of different thickness, a second set of samples (later referred as thin flakes) was produced under a two-step ball milling process at 1400 rpm, hexane and 2 wt% stearic acid were used as PCAs to evade excessive cold welding. First step consisted in milling for 2 h at a BPR of 40:1 with 1 mm zirconia balls for comminution, second step required a higher BPR of 60:1 during 0.5 h to produce the desired thin flakes.

2.2. Materials characterization

A JEOL JSM-6490LV scanning electron microscope (SEM) was used

to study the morphology of both the as-received and the milled powders (coarse and thin flakes) before and after hydrogen tests. Average size of the particles as well as the flake percentage (number of flakes relative to the total number of particles) were determined using the ImageJ software [38].

Microstructure of Mg-cp and flake-like powders were determined by X-ray diffraction (XRD) upon a PANalytical Empyrean Malvern diffractometer (Cu Kα radiation, 45 kV, 40 mA) scanning in the 2θ range of 20–80° with a 0.026° step, further crystalline phase identification was conducted using X'pert High Score Analysis software and ICSD database, crystallite size, lattice strain and dislocation density were determined using the Scherrer calculator tool from the aforementioned software and the methodology explained by Rios, J. et al. in Ref. [39], Goodness of Fit and Weighted R Profile values were kept under 4 and 10 respectively, to assess trustworthy results.

2.3. Hydrogen tests

Kinetics experiments were conducted in a Sievert's type apparatus designed and constructed by the researchers, consisting of one volume for the sample reaction and a reference volume similar to the one reported by Suárez-Alcántara et al. in [40]. Sorption and desorption reactions were conducted over 100–300 mg of sample which was charged/discharged under argon atmosphere to prevent oxygen poisoning of the materials. Tubing and reference reactor were purged with three argon-vacuum cycles before running the calibration and measurement processes. Calibration is required to determine the total void volume in the system for future calculations and is done by filling both tubing and reference reactor with argon (7 bar) at 100 °C, a simple calculation from pressure and temperature changes before and after communicating both the sample and the reference reactors is done through the ideal gas equation.

After proper calibration, an activation process was done at 400 °C during 6 h for sorption (20 bar) and 6 h for desorption (1 bar), this aimed to generate cracks on previously formed oxides or detach the oxide layer on the particles to expose pure Mg on the surface, facilitating direct contact with hydrogen during the tests. Afterwards, isothermal hydrogen sorption/desorption experiments were performed at 350 °C on both coarse and thin Mg flakes, as well as on commercially pure Mg for comparison. Heating was conducted once each sample was loaded in the analysis reactor, after reaching the isothermal condition at the desired temperature, a valve located between the sample and the reference reactor was opened to let a calculated aliquot of hydrogen expand in the void space, thus, allowing the hydrogenation process to happen, once a pressure stabilization occurred, i.e., an apparent equilibrium was reached, the reactor valve was closed and hydrogen in the reference reactor and tubing was released through a vacuum pump until reaching a pressure of 0.8 bar. Subsequently, all valves were closed and only the reactor valve was reopened to start the dehydrogenation process. Communication of the volumes resulted in a slight expansion of the gas, thereby, increasing the starting pressure for the desorption experiments to 1 bar.

Additional sorption tests at 300, 250 and 200 °C at 20 bar were conducted for thin flakes, desorption reactions were all performed at 350 °C and 1 bar of pressure. Another set of sorption tests were conducted at 350 °C and 300 °C at 10 bar to compare the Mg thin flakes performance at relatively low pressure against the previously tested pressure (20 bar). Pressure changes were recorded through a datalogger every second during the experiments, and data sets obtained were later used for wt.% H_2 uptake/release determination.

3. Results & discussion

3.1. Morphological characterization of materials

Morphology of the starting powders and particle size distribution can

Table 1
Parameters used during milling of magnesium particles for coarse flakes samples (125 ml jar, 300 rpm speed, BPR of 40:1).

Sample Name[a]	Milling Parameters			
	Zirconia ball size (mm)	Milling time (h)	Milling interval (min/min)	Process Control Agent, PCA
Z1T1i1:3H	1	1	5/15	Hexane
Z1T2i1:3H	1	2	5/15	Hexane
Z1T3i1:3H	1	3	5/15	Hexane
Z1T3i1:3H0.5SA	1	3	5/15	Hexane – 0.5 wt% SA
Z1T3i1:3H2SA	1	3	5/15	Hexane – 2.0 wt% SA
Z1T4i1:3H	1	4	5/15	Hexane
Z1T5i1:1H	1	5	10/10	Hexane
Z1T5i1:3	1	5	5/15	None
Z1T5i1:3H	1	5	5/15	Hexane
Z1T10i1:3H	1	10	5/15	Hexane
Z1T15i1:3H	1	15	5/15	Hexane
Z3T1i1:3H	3	1	5/15	Hexane
Z3T3i1:3H	3	3	5/15	Hexane
Z3T5i1:1H	3	5	10/10	Hexane
Z3T5i1:3H	3	5	5/15	Hexane
Z10T5i1:1H	10	5	10/10	Hexane

[a] Each letter in the sample name stands for each parameter used, Z is for zirconia ball size, T is for milling time, i for milling interval, H for hexane and SA for stearic acid used as PCAs.
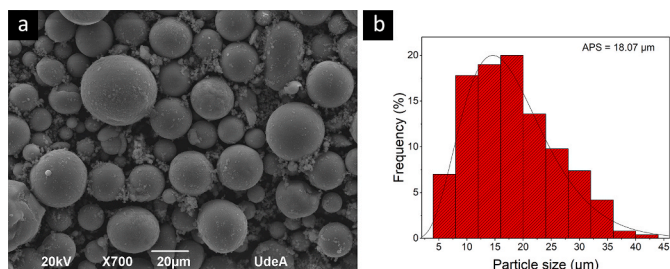
Fig. 1. As-received powders of commercially pure magnesium, secondary electron - SEM micrograph (a), and particle size distribution (b).

be observed in Fig. 1, the powders exhibited a spherical well-defined shape and Log-Normal monomodal distribution with an average particle size (APS) of 18.07 μm.

A study on the effect of different milling parameters in the production of magnesium coarse flakes was conducted to find conditions for the fabrication of flake contents above 70% in a sample. Among the parameters studied, milling time and surfactant assisted milling were the most significant parameters in producing the highest content of flakes, description of the effect of other parameters in flake morphology and content (ball size, milling-resting interval, hexane addition and ball size-time mixed effect) can be found on Supplementary material.

Variations described in sections S1, S2 and S3 from Supplementary material, such as 1 mm zirconia balls, a milling-resting interval of 1:3 and hexane as PCA were kept constant due to their interesting effect in the morphology of magnesium flakes with an APS of 32.88 ± 6.32 μm

and thickness of 1.72 ± 0.68 μm. Different milling times (1, 2, 3, 4, 5, 10 and 15 h) were tested to improve the flake content of the desired morphology in the powders, results are presented in Fig. 2. In general, the variation in average particle size was not significative as observed in Fig. 2a. Conversely, there were significant variations for the flake content by varying time, a peak of 73.00% of flakes appeared for the 2 h milled powder (Z1T2i1:3H), while the flake percentage started to decrease to values of 50.40%, 35.18%, 32.84%, 14.45%, 14.42% and 3.40% for samples milled at 3, 4, 5, 10, 1 and 15 h respectively, it can qualitatively be seen in the micrographs presented in Fig. 2b–h. At milling times as low as 1 h (Fig. 2b), little to no deformation or size reduction is observed due to insufficient energy transfer from the milling balls to the powders. However, with further milling (2 h), collisions between Mg powders and milling balls lead to material deformation and an increase in the flake content in the powders (Fig. 2c). Although Mg exhibits a brittle behavior due to its hexagonal closed packed structure which lacks twinning deformation and have few slip systems, it can be ductilized by activation of non-basal slip systems when refining the grain size by ball milling [41,42], in these type of processes an increase in localized temperature occurs, which could also improve ductility of HCP-Mg by promoting mobility of dislocations and activation of prismatic and pyramidal slip systems [2,43], which can explain the deformed Mg particles at 2 h of milling.

Further milling at longer times than 2 h, results in a repetitive agglomeration and fracture process that competes against the deformation of the particles. As a result, newly formed particles with a spherical shape become predominant over the flake-shaped particles (Fig. 2d–h).
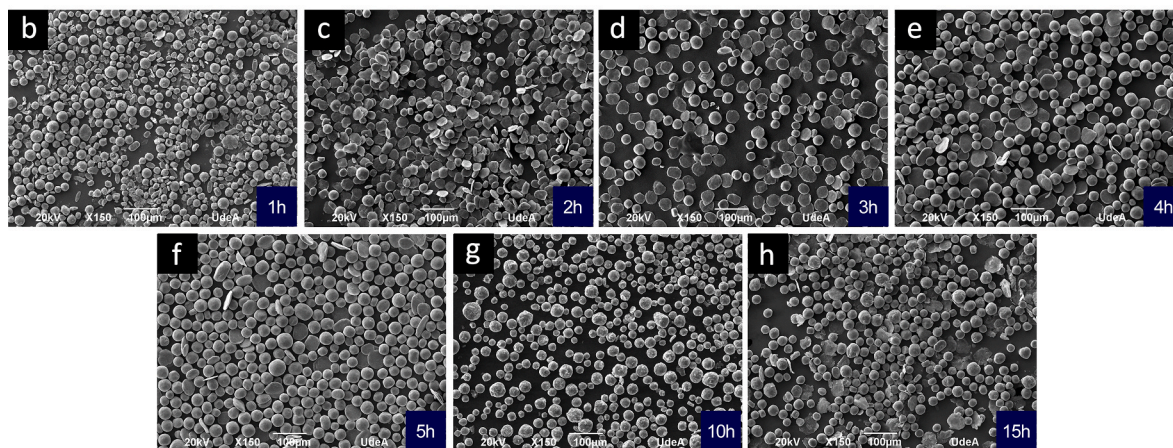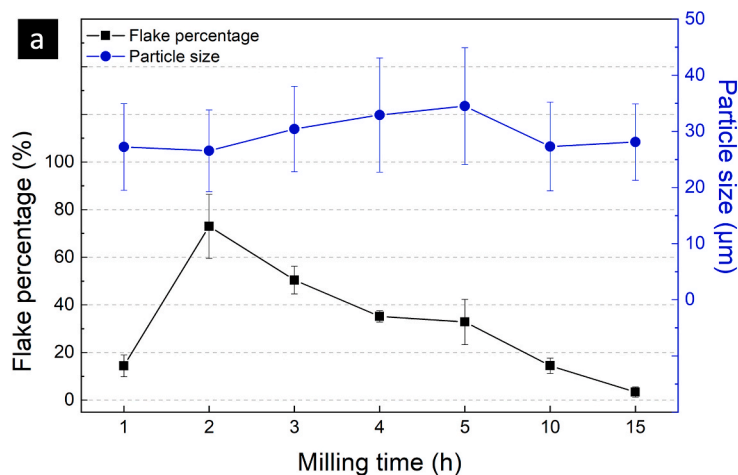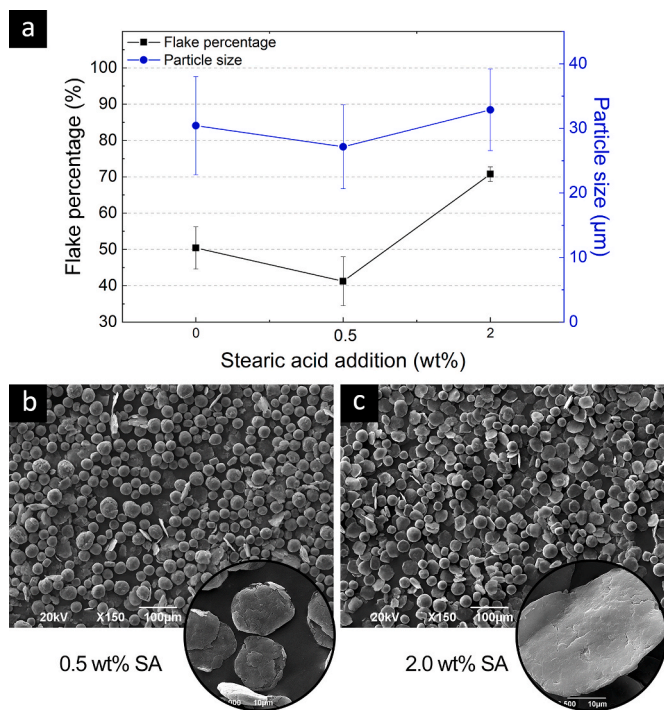

Fig. 2. Influence of milling time in the particle size and flake percentage of the particles milled under various times (a) and SE - SEM micrographs of samples Z1T1i1:3H (b), Z1T2i1:3H (c), Z1T3i1:3H (d), Z1T4i1:3H (e), Z1T5i1:3H (f), Z1T10i1:3H (g) and Z1T15i1:3H (h).

Fig. 3. Particle size and flake percentage for samples processed under surfactant assisted ball milling (a). SE - SEM micrographs of samples Z1T3i1:3H0.5SA (b) and Z1T3i1:3H2SA (c).

A surfactant such as stearic acid (SA), was added to hexane to evaluate its impact on flake production during ball milling. Fig. 3 displays the change in size, flake content and morphology of the samples processed at this stage. The addition of 0.5 %wt. of SA, resulted in a slight decrease in the flake percentage from 50.40% (sample Z1T3i1:3H) to 41.24% (sample Z1T3i1:3H0.5SA), while a significant increase to 70.74% was observed for sample Z1T3i1:3H2SA, milled with 2.0% of SA (Fig. 3a). This could be explained by studies where Surfactant Assisted Ball Milling (SA-BM) was applied [44–46], which propose that incorporating a surfactant agent like stearic acid or oleic acid and a liquid PCA such as hexane or heptane provides a dual effect of lubrication by creating a surfactant film around each particle that hinders particle-to-particle interaction during milling, thereby preventing excessive cold-welding and promoting particle deformation. The samples with SA addition displayed similar morphology (Fig. 3b and c), both

consisting of smooth spherical and flake-like particles, although the Z1T3i1:3H2SA sample had a greater number of flakes.

With the above-mentioned results, a brief mechanism of deformation is proposed to understand the evolution of the morphology of magnesium (Fig. 4). Two schematic routes are presented, both use similar parameters of high energy ball milling for c.p Mg powders (1 mm ZrO_2 balls, 300 rpm, BPR of 40:1, 1:3 milling interval), one of them uses only hexane as PCA and the other one uses a hexane-2 wt.% stearic acid mixture. In the hexane-only route, the particles start to deform in a micro-rolling process that occurs between the starting powders and the milling balls as stated by Sadeghi, B. & Cavaliere, P in [21]. At 1 h of milling, there is not enough energy transferred to the material, so little to no deformation neither size reduction are observed; However, increasing the time around 2 h leads to a thorough deformation of the material as a result of the collisions and rolling between the ductilized powders of magnesium and the zirconia milling balls [2,21], generating a percentage of flakes higher than 70%. At further milling times ($t_m > 3$ h) there is additional energy that is allocated to other processes such as agglomeration, re-welding and fracture of the powders [11], which occur repetitively and compete against the deformation process, leading to a decrease in flake content, a refinement of the microstructure caused by plastic deformation, and the formation of new spherical-shaped particles with a similar size to that of the starting powders, this was due to the almost mandatory use of wet milling for Mg because of its high reactivity to prevent it from sticking to the jar walls and balls surface [47], which in combination with the low milling speeds (300 rpm) inhibited further comminution of the particles. In the second route, the addition of 0.5 wt% of stearic acid caused a decrease in flake content possibly because this quantity is not enough to create a thin film around the Mg particles. In contrast, a 2 wt% stearic acid promotes the formation of a thin layer around each particle, as a result of polar groups from SA being adsorbed onto freshly generated surfaces, since non-polar groups repulse against each other; cold-welding, agglomeration and subsequent fracture is prevented [48,49], leading to a higher content of flake-like magnesium.

Understanding the formation mechanism of the abovementioned flakes, specifically those in sample Z1T3i1:3H2SA (from now on "Mg coarse flakes"), an effort to reduce flake particle size and thickness was done, among the many strategies used, a two-step ball milling method was the most effective alternative. A first step of milling was conducted to comminute the particles and induce defects to activate deformation planes and increase dislocation density before the actual deformation as Rios et al. stated in Ref. [39]. In Fig. 5a, finer particles than the starting material with an average particle size of 9.44 ± 4.72 μm and an irregular shape were obtained, DRX analysis confirmed the grain refining and
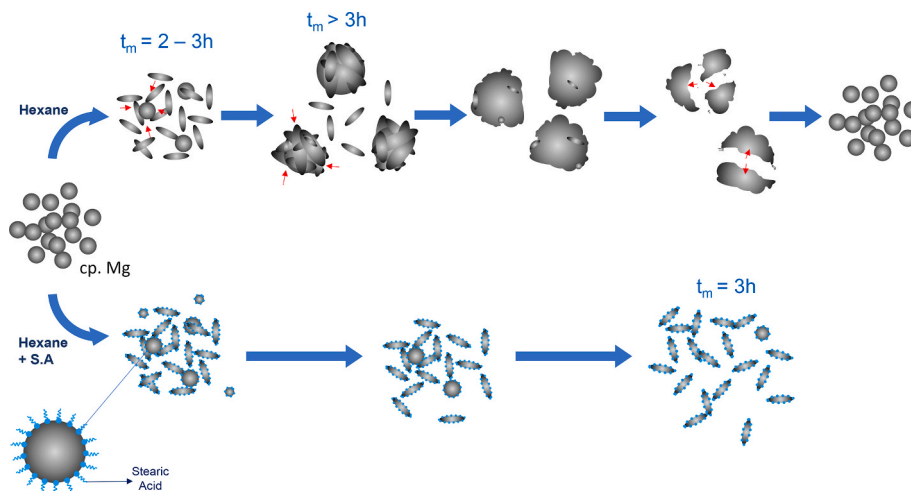
Fig. 4. Schematic representation of the flake-like particles formation mechanism for magnesium powders at low milling speed (300 rpm).
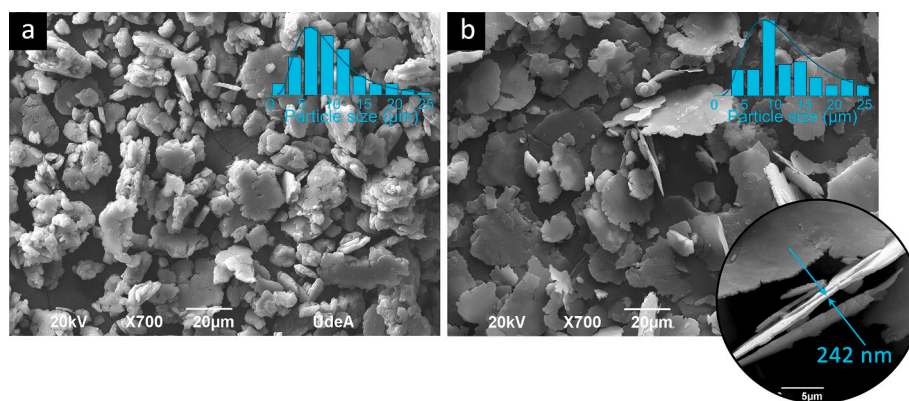
Fig. 5. SE - SEM images of Mg particles after (a) first step and (b) second step of thin-flakes synthesis through SA-BM.

Table 2
Results from Scherrer Analysis conducted on XRD patterns of c.p Mg and milled samples.

Sample	FWHM (°)	Crystallite size (nm)	Lattice Strain (%)	Dislocation density (x10^{14} m^{-2})
c.p Mg	0.0920	197.9	0.065	0.43
Mg Coarse flakes	0.1395	77.5	0.152	2.59
Mg Thin flakes (1st step)	0.3220	26.6	0.425	21.11
Mg Thin flakes (2nd step)	0.4220	17.8	0.633	46.91

dislocation density increase by Scherrer analysis (Table 2).

Mg thin flakes were obtained after a second step of milling, where high deformation was expected since there were already activated slip planes, producing flakes with an APS of 12.89 ± 7.47 μm and a thickness of 242 ± 72 nm, as seen in Fig. 5b.

3.2. Microstructural analysis

XRD analysis was conducted on starting powders (c.p Mg) and both Mg coarse flakes (Fig. 3c) and Mg thin flakes (Fig. 5b) to elucidate if a microstructural change took place during the ball milling process in one or two-steps. Fig. 6 displays the diffractograms obtained, all samples had the same reference pattern fitting (ICSD 98-007-7908), showing characteristic magnesium peaks at $2\theta = 32.18°$, $34.40°$ and $36.62°$ corresponding to the planes (010), (002) and (011) of hcp-Mg, respectively.
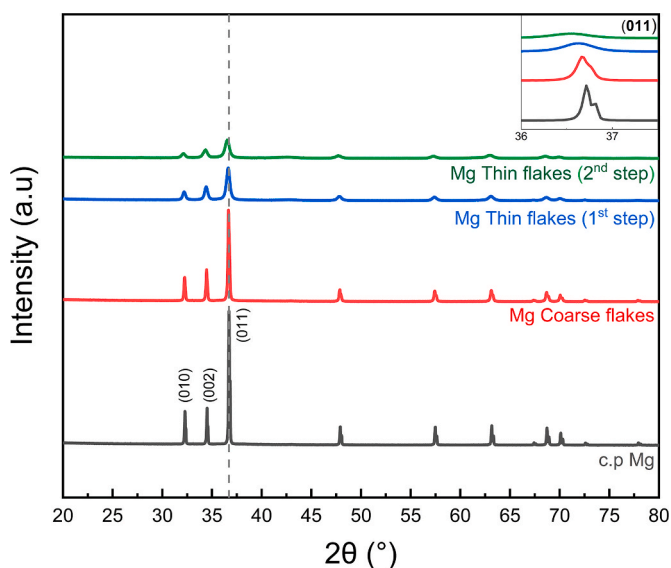
Fig. 6. XRD patterns of commercially pure Mg (c.p Mg), Mg coarse flakes (Z1T2i1:3H sample), first and second step of milling for Mg Thin-flakes production.

The position of the peaks had no significant change when comparing Mg coarse flakes spectra with commercially pure sample, indicating that the hexagonal structure was retained. Nevertheless, a slightly displacement was observed for both steps of Mg thin flakes formation, which agrees with the higher lattice strain compared to that of c.p Mg (Table 2). Additionally, broadening of the main peak occurred for the milled samples as seen in the inset of Fig. 6, which was later confirmed with the Full Width at Half Maximum (FWHM) measurements presented in the same table; indicating that a microstructural refinement with ball milling of the c.p Mg took place and led to a nanostructured material after the milling process as reported elsewhere [39]. Hence, reductions of 60.8%, 86.5% and 91.0% in crystallite size were observed when milling at 2 h/300 rpm (Mg coarse flakes), 2 h/1400 rpm (1st step Mg thin flakes) and 0.5 h/1400 rpm (2nd step Mg thin flakes) respectively, this reduction is attributed to the severe deformation induced by ball milling and an increase in the nucleation sites resulting from a higher density of dislocations generated during the collisions between the powders and the milling balls [42,50].

3.3. Hydrogen storage performance

After activation process, isothermal kinetic tests were conducted on the samples, both thin and coarse flakes were evaluated against c.p Mg. As seen from the results presented in Fig. 7a, flakes performed better than c.p Mg in sorption tests at 350 °C/20 bar, with higher capacities and lower times for reaching those values. Specifically, a hydrogen storage capacity of 4.6 wt% was reached after 6 min for thin flakes, followed by 4.1 wt% achieved by the coarse flakes after 60 min of hydrogenation, in contrast, c.p Mg presented the lowest capacity (3.4 wt%) at the longest time (100 min). This improvement in capacity can be attributed to the nanostructured nature of both type of flakes as mentioned in the microstructural analysis (Section 3.2), which constitutes more nucleation sites for the formation of magnesium hydride and diffusion of hydrogen through smaller structures within the material, allowing a higher hydrogenated volume of the particle and improved kinetics [51,52]. Additionally, the thickness play an important role in the kinetics of sorption due to shorter diffusion pathways for the hydrogen in one dimension (thickness of flakes) [40], this goes in agreement with the difference in sizes among both types of flakes, where
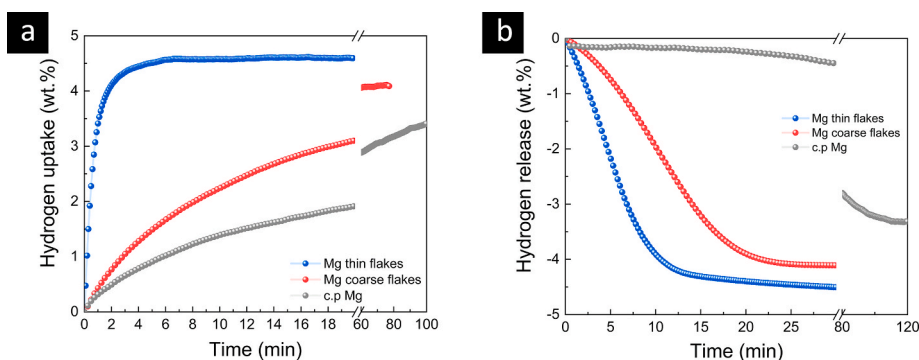
Fig. 7. Kinetics of sorption (a) and desorption (b) for the three materials tested at 350 °C.
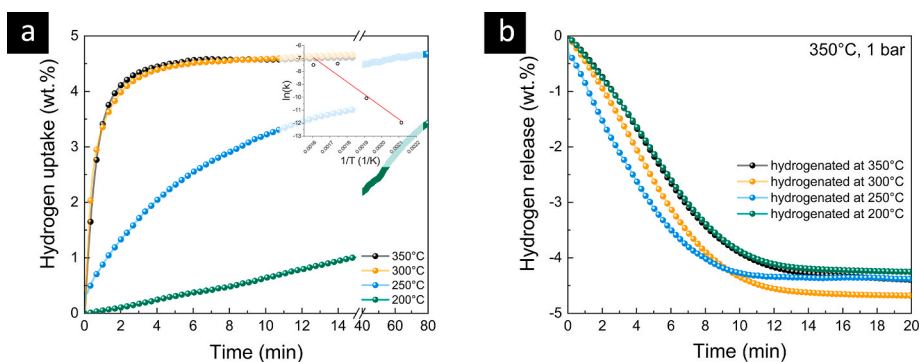
Fig. 8. Kinetics of (a) sorption at different temperatures, 20 bar and (b) desorption at 350 °C, 1 bar of Mg thin flakes.

Table 3
Results from the kinetics model fitting.

Model	Equation[a]	Adjusted R^2	Activation Energy (kJ/mol)
JMA – 3D	$[-\ln(1-Y)]^{1/3} = kt$	0.96171	110.6 ± 22.9
JMA – 2D	$[-\ln(1-Y)]^{1/2} = kt$	0.97349	79.1 ± 17.6
CV-Diffusion	$1 - \left(\dfrac{2Y}{3}\right) - (1-Y)^{\frac{2}{3}} = kt$	**0.99844**	**80.2 ± 16.6**

[a] Y = fraction of Mg transformed to MgH_2; k = kinetic constant at a given temperature; t = time.

thin flakes present thicknesses in the submicron scale and coarse flakes in the micron scale, further deformation could lead to thinner particles with thicknesses in the nanometric scale, which could achieve both higher capacities and faster kinetics of absorption as seen in 2D particles of other hydrogen storage materials, due to the higher surface to volume ratio [23,53]. As expected, desorption processes were slower than sorption ones (Fig. 7b), due to the thermodynamic stability and sluggish kinetics of the already formed MgH_2 [54]. However, improvements in

kinetics of dehydrogenation were also observed for the flakes, with complete hydrogen desorption at 30 min for both types of flakes, while c.p Mg took more than 120 min to completely desorb.

Fig. 8 displays results from isotherms at different temperatures of Mg thin flakes, a drop in sorption kinetics is observed with a decrease in temperature (Fig. 8a), except for samples at 350 °C and 300 °C which behaved similarly and reached capacities of 4.6 wt% and 4.5 wt% at 6 min, respectively. A sample evaluated at 250 °C reached a similar
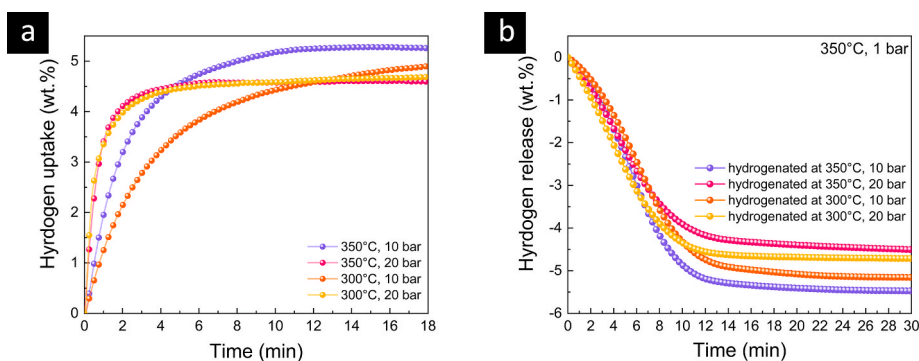
Fig. 9. Kinetics of sorption (a) and desorption (b) of Mg thin flakes at 20 and 10 bar.
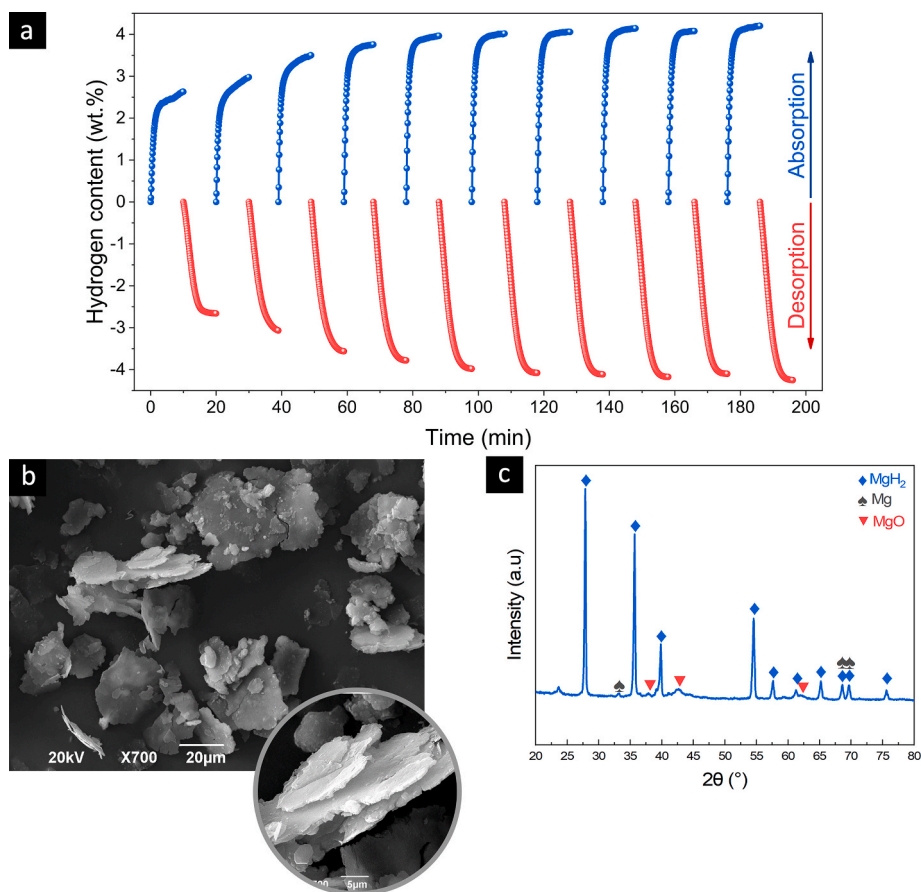
Fig. 10. Cycling test of Mg thin flakes (a), SE - SEM analysis (b) and XRD spectra (c) after 10 cycles of hydrogenation/dehydrogenation.

capacity of about 4.5 wt% after 50 min. Dehydrogenation was tested at temperatures below 350 °C; However, changes in pressure were not observed after 6 h at 300 °C, leading to no release of hydrogen, same for test at 250 °C. Hence, all desorption tests were conducted at 350 °C and 1 bar to assess complete desorption (Fig. 8b). All samples behaved analogously in desorption tests with times for complete release of hydrogen in the range of 12–15 min, slight differences in total hydrogen release were observed and they follow the values of previously absorbed hydrogen.

A kinetics analysis was conducted on the sorption isotherms. Models that follow the nucleation and growth principle were used: the Johnson-Mehl-Avrami considering two (JMA-2D) and three dimensional (JMA-3D) growth of the new phase, and the contracting volume model with three-dimensional diffusion-controlled growth (CV-Diffusion). Calculations were performed following the procedure described in Refs. [40, 55]. Briefly, kinetics curves were fitted using the three models in order to calculate kinetic constants (k) from the slope of these curves. Therefore, all k's were plotted against the inverse of temperature for all the models evaluated (Fig. S4, supplementary material) and activation energy was computed from the slope of the linear fitting of these graphs; results as well as the models equations are presented in Table 3.

Both JMA-2D and CV-Diffusion models presented a good fitting (inset Fig. 8a) with the adjusted R-square values closest to 1 (Table 3). Nevertheless, residuals were lower for CV-Diffusion compared to JMA-2D model, leading to conclude that the best fit was the diffusion controlled model, which indicates that the rate limiting step for the hydrogenation of Mg thin flakes from 200 to 350 °C, is the diffusion of hydrogen through the newly formed MgH_2 phase [40,55]. According to this model, activation energy for sorption was 80.2 ± 16.6 kJ/mol for

the Mg thin flakes, which goes in agreement with the kinetic results performance of the material compared to pristine Mg, whose activation energy is in the range of 95–130 kJ/mol according to literature [56–58].

Due to the similar behavior of Mg thin flakes at 350 °C and 300 °C, additional tests were performed varying the pressure from 20 to 10 bar at both temperatures, these tests aimed to identify performance under lower pressure conditions. Although Mg thin flakes presented slower kinetics at 10 bar compared to the previous tests, due to a lower driving force of the hydrogen sorption reaction as a result of a pressure closer to the equilibrium pressure of pure Mg (4 bar at 360 °C) that leads to slower rate of sorption [59,60]. Higher capacities were also achieved in comparison to those exhibited at 20 bar (Fig. 9), this goes in agreement with Tien et al. [61], who states that a small difference between temperature of the test and equilibrium temperature at a given pressure could lead to higher capacities thanks to the formation of few nuclei on the surface that then grow until almost complete hydrogenation of the particle. In contrast, when the difference is bigger, the kinetics of nucleation are faster and more nuclei are formed before the growing stage, leading to faster coalescence of the MgH_2 formed that prevents the diffusion of hydrogen to complete hydrogenation of the particle.

Equilibrium temperature for MgH_2 reaction at 20 bar is about 403 °C, while at 10 bar decreases to 367 °C [62] and both test temperatures (350 and 300 °C) are closer to the later one than to the equilibrium temperature at 20 bar. However, lowering the pressure of the test to 10 bar implies a reduction in the driving force that accelerates the kinetics of hydrogenation [62,63], leading to sorption values of 5.3 wt% in 12 min and 4.9 wt% in 16 min for tests at 350 °C/10 bar and 300 °C/10 bar, respectively. This also helped to elucidate the rate-limiting stages at different pressures. At 20 bar, the rapid formation of the MgH_2 layer,

seen as a fast absorption until 4 min (Fig. 9), led to the rate-limiting step which was the slow process of hydrogen diffusion through the hydride layer. In contrast, the slow nucleation process in the samples evaluated at 10 bar, exhibited a faster rate after 4 min compared to those tested at 20 bar, in this case, the rate limiting step was the growth of the nucleated phase because of the low driving force of reaction [8,64].

When comparing values of maximum capacity over the time to achieve it for the four set of conditions, Mg thin flakes performed better at 350 °C/20 bar and 300 °C/20 bar than at 350 °C/10 bar and 300 °C/ 10 bar, althought the latter have potential for practical applications due to the operational conditions and the increased hydrogen capacity, additional modifications such as alloying or using other additives could help to improve kinetics as seen in other studies [32,40,65–67].

Finally, to evaluate the cyclability of Mg thin flakes, a repetitive hydrogenation/dehydrogenation test was conducted at 350 °C and 20 bar. From the results presented in Fig. 10a, an additional activation was observed in the first three cycles, with a hydrogen storage capacity of 4.2 wt% achived after 10 cycles. The material exhibited stable hydrogen sorption/desorption behavior, showing an increased capacity with each cycle. Further tests are required to determine the cycle at which a decrease in hydrogen storage capacity occurs. SEM analysis conducted after the tests revealed that the flake-like morphology was preserved (Fig. 10b). This preservation could provide an additional advantage of using micrometric flakes with submicron thickness over 3D nanoparticles; The latter tend to agglomerate and cold weld with cycling, resulting in the loss of their interesting nanoscale properties [52,68]. XRD spectra presented in Fig. 10c, evidenced the MgH_2 formation after cycling and hydriding, a substantial part of Mg was transformed to its hydrided form as characteristic peaks at $2\theta = 27.91, 35.73, 39.88$ and $54.61°$ were observed according to the ICSD-98-002-6624 pattern. A few peaks of unreacted Mg were also identified, along with peaks associated to MgO formation. This occurrence was inevitable due to the sample's exposure to oxygen for a brief period of time (about 10 s) during XRD analysis.

4. Conclusions

Different magnesium flakes were successfully obtained from milling of commercially pure Mg using an Emax high energy ball mill, process in one or two step led to coarse and thin flakes, respectively. Among the many parameters evaluated, low milling times (2–3 h) and the use of hexane + stearic acid as PCAs promoted the formation of highest content (>70%) of coarse flakes with ~1.72 μm thickness and APS of ~32.88 μm. The two-step process led to the formation of finer and thinner flakes, thanks to the comminution and activation of slip planes in the first step and the further deformation in the second step.

The hydrogen storage performance of Mg flakes was assessed through isothermal kinetic tests at 350 °C and 20 bar, revealing that an increase in kinetics was achieved by reducing thickness of the flakes, thinner flakes exhibited faster sorption/desorption rates, reaching a capacity of 4.6 wt% after 6 min of hydrogenation; even at 300 °C, Mg thin flakes achieved 4.5 wt% of hydrogen uptake in 6 min microstructural changes were also evidenced in the flake formation, a decrease in crystallite size with increased milling time resulted in improved hydrogen storage capacities and kinetics, lower testing pressure of 10 bar increase capacity as well at expenses of slower kinetics. Among the highlights of this work, Mg thin flakes presented a high cyclic stability and preserved morphology after 10 hydrogenation/dehydrogenation cycles.

The enhanced performance of Mg thin flakes in sorption/desorption tests makes them a suitable starting material for hydrogen storage applications, other modification techniques such as alloying with transition metals can be used to improve storage properties such as thermodynamics of hydrogenation/dehydrogenation.

CRediT authorship contribution statement

Joan S. Cortinez: Writing – original draft, Visualization, Methodology, Investigation, Formal analysis, Data curation. **Alejandro Gómez:** Validation, Software, Methodology. **Alejandro A. Zuleta Gil:** Writing – review & editing, Supervision, Methodology. **José A. Tamayo:** Writing – review & editing. **Esteban Correa:** Writing – review & editing, Supervision, Methodology. **Francisco J. Bolívar:** Supervision, Resources, Conceptualization. **Félix Echeverría Echeverria:** Writing – review & editing, Supervision, Project administration, Funding acquisition, Conceptualization.

Declaration of competing interest

The authors declare that they have no known competing financial interests or personal relationships that could have appeared to influence the work reported in this paper.

Appendix A. Supplementary data

Supplementary data to this article can be found online at https://doi. org/10.1016/j.ijhydene.2024.05.254.

References

[1] Pighin SA, Urretavizcaya G, Bobet JL, Castro FJ. Nanostructured Mg for hydrogen production by hydrolysis obtained by MgH2 milling and dehydriding. J Alloys Compd 2020;827:154000. https://doi.org/10.1016/j.jallcom.2020.154000.

[2] Galindez Y, Correa E, Zuleta AA, Valencia-Escobar A, Calderon D, Toro L, et al. Improved Mg–Al–Zn magnesium alloys produced by high energy milling and hot sintering. Met Mater Int 2021;27:1113–30. https://doi.org/10.1007/s12540-019-00490-1.

[3] Kang M, Dixit N, Hazeli K, Xie K, Hemker K, Ramesh KT. The mechanical behavior of single crystal and polycrystalline pure magnesium. Mech Mater 2021;163. https://doi.org/10.1016/j.mechmat.2021.104078.

[4] Ratna Sunil B, Ganapathy C, Sampath Kumar TS, Chakkingal U. Processing and mechanical behavior of lamellar structured degradable magnesium-hydroxyapatite implants. J Mech Behav Biomed Mater 2014;40:178–89. https://doi.org/10.1016/j.jmbbm.2014.08.016.

[5] Esmaily M, Svensson JE, Fajardo S, Birbilis N, Frankel GS, Virtanen S, et al. Fundamentals and advances in magnesium alloy corrosion. Prog Mater Sci 2017;89:92–193. https://doi.org/10.1016/j.pmatsci.2017.04.011.

[6] Hitam CNC, Aziz MAA, Ruhaimi AH, Taib MR. Magnesium-based alloys for solid-state hydrogen storage applications: a review. Int J Hydrogen Energy 2021;46:31067–83. https://doi.org/10.1016/j.ijhydene.2021.03.153.

[7] Li X, Yuan Z, Liu C, Sui Y, Zhai T, Hou Z, et al. Research progress in improved hydrogen storage properties of Mg-based alloys with metal-based materials and light metals. Int J Hydrogen Energy 2024;50:1401–17. https://doi.org/10.1016/j.ijhydene.2023.09.265.

[8] Sui Y, Yuan Z, Zhou D, Zhai T, Li X, Feng D, et al. Recent progress of nanotechnology in enhancing hydrogen storage performance of magnesium-based materials: a review. Int J Hydrogen Energy 2022;47:30546–66. https://doi.org/10.1016/j.ijhydene.2022.06.310.

[9] Esamael SK, Fatalla AA. Evaluation on processing parameter's effects on some mechanical properties of pure magnesium bulk prepared by powder metallurgy. Mater Today Proc 2022. https://doi.org/10.1016/j.matpr.2022.02.016.

[10] Březina M, Minda J, Doležal P, Krystýnová M, Fintová S, Zapletal J, et al. Characterization of powder metallurgy processed pure magnesium materials for biomedical applications. Metals 2017;7:1–22. https://doi.org/10.3390/met7110461.

[11] Suryanarayana C. Mechanical alloying and milling. Prog Mater Sci 2001;46:1–184. https://doi.org/10.1016/S0079-6425(99)00010-9.

[12] Mukhtar S, Kamran M, Ahmed R, Tayyeb A. Effect of milling parameters on mechanical properties and in vitro biocompatibility of Mg-Zn-Co ternary alloy. Metals 2022;12:1–13. https://doi.org/10.3390/met12030529.

[13] Park K, Park J, Kwon H. Effect of intermetallic compound on the Al-Mg composite materials fabricated by mechanical ball milling and spark plasma sintering. J Alloys Compd 2018;739:311–8. https://doi.org/10.1016/j.jallcom.2017.12.054.

[14] Rattan Paul D, Sharma A, Panchal P, Chaudhary S, Patidar D, Nehra SP. Effect of ball milling and iron mixing on structural and morphological properties of magnesium for hydrogen storage application. Mater Today Proc 2019;42:1673–7. https://doi.org/10.1016/j.matpr.2020.08.035. Elsevier Ltd.

[15] Berezovets VV, Denys RV, Zavaliy IY, Kosarchyn YV. Effect of Ti-based nanosized additives on the hydrogen storage properties of MgH2. Int J Hydrogen Energy 2022;47:7289–98. https://doi.org/10.1016/j.ijhydene.2021.03.019.

[16] Strozi RB, Leiva DR, Huot J, Botta WJ, Zepon G. An approach to design single BCC Mg-containing high entropy alloys for hydrogen storage applications. Int J Hydrogen Energy 2021;46:25555–61. https://doi.org/10.1016/j.ijhydene.2021.05.087.

[17] Liu X, Wu S, Cai X, Zhou L. Hydrogen storage behaviour of Cr- and Mn-doped Mg2Ni alloys fabricated via high-energy ball milling. Int J Hydrogen Energy 2023; 48:17202–15. https://doi.org/10.1016/j.ijhydene.2023.01.180.

[18] Chen H, Xiao H, Wang Y, Liu J, Yang Q, Feng X. Insight into the energy conversion and structural evolution of magnesium hydride during high-energy ball milling for its controllable synthesis. J Alloys Compd 2020;836:155312. https://doi.org/10.1016/j.jallcom.2020.155312.

[19] Minárik P, Zemková M, Kozlík J, Lukáč F, Král R. Effect of flake-like powder morphology on the microstructure and texture in Mg-Al-RE alloy. Mater Lett 2020; 262:127031. https://doi.org/10.1016/j.matlet.2019.127031.

[20] Varol T, Canakci A. The effect of type and ratio of reinforcement on the synthesis and characterization Cu-based nanocomposites by flake powder metallurgy. J Alloys Compd 2015;649:1066–74. https://doi.org/10.1016/j.jallcom.2015.07.008.

[21] Sadeghi B, Cavaliere P. Progress of flake powder metallurgy research. Metals 2021; 11:1–15. https://doi.org/10.3390/met11060931.

[22] Varol T, Canakci A, Ozsahin S. Prediction of effect of reinforcement content, flake size and flake time on the density and hardness of flake AA2024-SiC nanocomposites using neural networks. J Alloys Compd 2018;739:1005–14. https://doi.org/10.1016/j.jallcom.2017.12.256.

[23] Alharthi NH, Almotairy SM, Almutairi AM. Frictional behavior and mechanical performance of Al reinforced with SiC via novel flake powder metallurgy. Metals 2022;12. https://doi.org/10.3390/met12020323.

[24] Sippel TR, Son SF, Groven LJ. Aluminum agglomeration reduction in a composite propellant using tailored Al/PTFE particles. Combust Flame 2014;161:311–21. https://doi.org/10.1016/j.combustflame.2013.08.009.

[25] Akhlaghi F, Zare-Bidaki A. Influence of graphite content on the dry sliding and oil impregnated sliding wear behavior of Al 2024-graphite composites produced by in situ powder metallurgy method. Wear 2009;266:37–45. https://doi.org/10.1016/j.wear.2008.05.013.

[26] Yan SJ, Dai SL, Zhang XY, Yang C, Hong QH, Chen JZ, et al. Investigating aluminum alloy reinforced by graphene nanoflakes. Mater Sci Eng A 2014;612: 440–4. https://doi.org/10.1016/j.msea.2014.06.077.

[27] Jiang L, Li J, Fan G, Cao L, Zhang D. The use of flake powder metallurgy to produce carbon nanotube (CNT)/aluminum composites with a homogenous CNT distribution. Carbon N Y 2012;50:1993–8. https://doi.org/10.1016/j.carbon.2011.12.057.

[28] Khorashadizade F, Abazari S, Rajabi M, Bakhsheshi-Rad HR, Ismail AF, Sharif S, et al. Overview of magnesium-ceramic composites: mechanical, corrosion and biological properties. J Mater Res Technol 2021;15:6034–66. https://doi.org/10.1016/j.jmrt.2021.10.141.

[29] Fallatah AM, Owidah ZO, Elsabawy KM. Synthesis of newly non-crystalline-porous-2D-flakes- Mg(II) -methyl 3, 5-dinitro-salicylate complex for hydrogen storage. J Mol Struct 2021;1238:130415. https://doi.org/10.1016/j.molstruc.2021.130415.

[30] Ruiz-Navas EM, Edil da Costa C, Velasco López F, Torralba Castelló JM. Mechanical alloying: a method to obtain metallic powders and composite materials. Rev Metal (Madr) 2000;36:279–86. https://doi.org/10.3989/revmetalm.2000.v36.i4.578.

[31] Babić B, Prvulović M, Filipović N, Mravik Ž, Sekulić Z, Govedarović SM, et al. Hydrogen storage properties of MgH2–Tm: Ni-catalysis vs. mechanical milling. Int J Hydrogen Energy 2024;54:446–56. https://doi.org/10.1016/j.ijhydene.2023.04.078.

[32] Zhang Z, He D, Xing X, Liu Y, Liu T. Al and Zr addition to improve the hydrogen storage kinetics of Mg-based nanocomposites: synergistic effects of multiphase nanocatalysts. J Alloys Compd 2023;942:169098. https://doi.org/10.1016/j.jallcom.2023.169098.

[33] Salehabadi A, Dawi EA, Sabur DA, Al-Azzawi WK, Salavati-Niasari M. Progress on nano-scaled alloys and mixed metal oxides in solid-state hydrogen storage; an overview. J Energy Storage 2023;61:106722. https://doi.org/10.1016/j.est.2023.106722.

[34] Wang P, Tian Z, Wang Z, Xia C, Yang T, Ou X. Improved hydrogen storage properties of MgH2 using transition metal sulfides as catalyst. Int J Hydrogen Energy 2021;46:27107–18. https://doi.org/10.1016/j.ijhydene.2021.05.172.

[35] Lu H, Li J, Xie T, Chen Y, Lu Y, Liu Z, et al. Mg/MgH2 hydrogen storage system destabilized by recyclable AlH3–NaBH4 composite. Int J Hydrogen Energy 2022; 47:35737–46. https://doi.org/10.1016/j.ijhydene.2022.08.156.

[36] Liu X, Wu S, Cai X, Zhou L. Hydrogen storage behaviour of Cr- and Mn-doped Mg2Ni alloys fabricated via high-energy ball milling. Int J Hydrogen Energy 2023; 48:17202–15. https://doi.org/10.1016/j.ijhydene.2023.01.180.

[37] Rathi B, Agarwal S, Shrivastava K, Kumar M, Jain A. Recent advances in designing metal oxide-based catalysts to enhance the sorption kinetics of magnesium hydride. Int J Hydrogen Energy 2024;53:131–62. https://doi.org/10.1016/j.ijhydene.2023.12.031.

[38] Schneider CA, Rasband WS, Eliceiri KW. NIH Image to ImageJ: 25 years of image analysis. Nat Methods 2012;9:671–5. https://doi.org/10.1038/nmeth.2089.

[39] Rios JM, Restrepo AH, Zuleta AA, Javier Bolívar F, Castaño JG, Correa E, et al. Effects of two-step high-energy ball milling process and hot isostatic pressing on the mechanical properties of PM magnesium. Int J Adv Manuf Technol 2022;121: 187–96. https://doi.org/10.1007/s00170-022-09299-6.

[40] Suárez-Alcántara K, Flores-Jacobo NI, Osorio-García M del P, Cabañas-Moreno JG. Fast hydrogen sorption kinetics in Mg-VCl3 produced by cryogenic ball-milling. Materials 2023;16. https://doi.org/10.3390/ma16062526.

[41] Shu BP, Liu L, Shen B, Hu WB. Deformation twinning in ultra-fine grained Ni at room temperature and low strain rate. Mater Lett 2013;91:268–71. https://doi.org/10.1016/j.matlet.2012.10.027.

[42] Rios J, Restrepo A, Zuleta A, Bolívar F, Castaño J, Correa E, et al. Effect of ball size on the microstructure and morphology of mg powders processed by high-energy ball milling. Metals 2021;11:1–10. https://doi.org/10.3390/met11101621.

[43] Chaudry UM, Hamad K, Kim JG. On the ductility of magnesium based materials: a mini review. J Alloys Compd 2019;792:652–64. https://doi.org/10.1016/j.jallcom.2019.04.031.

[44] Pal SK, Schultz L, Gutfleisch O. Effect of milling parameters on SmCo5 nanoflakes prepared by surfactant-assisted high energy ball milling. J Appl Phys 2013;113. https://doi.org/10.1063/1.4773323.

[45] Nie J, Han X, Du J, Xia W, Zhang J, Guo Z, et al. Structure and magnetism of SmCo5 nanoflakes prepared by surfactant-assisted ball milling with different ball sizes. J Magn Magn Mater 2013;347:116–23. https://doi.org/10.1016/j.jmmm.2013.06.047.

[46] Yu N, Pan M, Zhang P, Ge H, Wu Q. Effect of milling time on the morphology and magnetic properties of SmCo5 nanoflakes fabricated by surfactant-assisted high-energy ball milling. J Magn Magn Mater 2015;378:107–11. https://doi.org/10.1016/j.jmmm.2014.09.079.

[47] Synthesis techniques for magnesium-based materials. Magnesium, magnes. Alloy. Magnes Compos 2011:13–38. https://doi.org/10.1002/9780470905098.ch2.

[48] Thang NV, Van Dijk NH, Brück E. Effects of milling conditions on nano-scale MnFe (P,Si) particles by surfactant-assisted high-energy ball milling. Phys Procedia 2015; 75:1104–11. https://doi.org/10.1016/j.phpro.2015.12.183.

[49] Rocha CJ, Leal Neto RM, Gonçalves VS, Carvalho LL, Ambrozio Filho F. An investigation of the use of stearic acid as a process control agent in high energy ball milling of Nb-Al and Ni-Al powder mixtures. Mater Sci Forum 2003;416–418: 144–9. https://doi.org/10.4028/www.scientific.net/msf.416-418.144.

[50] Abu-Oqail A, Wagih A, Fathy A, Elkady O, Kabeel AM. Effect of high energy ball milling on strengthening of Cu-ZrO2 nanocomposites. Ceram Int 2019;45:5866–75. https://doi.org/10.1016/j.ceramint.2018.12.053.

[51] Guo F, Zhang T, Shi L, Chen Y, Song L. Mechanisms of hydrides' nucleation and the effect of hydrogen pressure induced driving force on de-/hydrogenation kinetics of Mg-based nanocrystalline alloys. Int J Hydrogen Energy 2022;47:1063–75. https://doi.org/10.1016/j.ijhydene.2021.10.104.

[52] Sadhasivam T, Kim HT, Jung S, Roh SH, Park JH, Jung HY. Dimensional effects of nanostructured Mg/MgH2 for hydrogen storage applications: a review. Renew Sustain Energy Rev 2017;72:523–34. https://doi.org/10.1016/j.rser.2017.01.107.

[53] Kalwar BA, Fangzong W, Rafique M, Soomro AM, Ahmed Z, Ahmed I. Enhanced storage capacity of hydrogen based on Li-decorated 2D BC6N under ambient conditions: first-principles study. Comput Mater Sci 2024;231:112621. https://doi.org/10.1016/j.commatsci.2023.112621.

[54] Nogita K, Tran XQ, Yamamoto T, Tanaka E, McDonald SD, Gourlay CM, et al. Evidence of the hydrogen release mechanism in bulk MgH2. Sci Rep 2015;5:1–5. https://doi.org/10.1038/srep08450.

[55] Zhu W, Yang H, Xu J, Yue S, Wang L, Liu J, et al. Function mechanism of Fe in improving cycle stability and plateau characteristics of AB5-type hydrogen storage alloys. Int J Hydrogen Energy 2024;63:1013–24. https://doi.org/10.1016/j.ijhydene.2024.03.231.

[56] Li H, Zhang Q, Chong C, Yap R, Tay K, Hang T, et al. Ac ce pte d M us pt. Mater Today Proc 2019;22:16–20.

[57] Rathi B, Agarwal S, Shrivastava K, Kumar M, Jain A. Recent advances in designing metal oxide-based catalysts to enhance the sorption kinetics of magnesium hydride. Int J Hydrogen Energy 2024;53:131–62. https://doi.org/10.1016/j.ijhydene.2023.12.031.

[58] Duan C, Su Z, Tian Y, Fu D, Zhang Y, Lv W, et al. Mechanochemical assisted hydrogenation of Mg-CNTs-Ni:kinetics modeling and reaction mechanism. Chem Eng J 2022;441:136059. https://doi.org/10.1016/j.cej.2022.136059.

[59] Züttel A. Hydrogen storage methods. Naturwissenschaften 2004;91:157–72. https://doi.org/10.1007/s00114-004-0516-x.

[60] Wang Y, Lü S, Zhou Z, Zhou W, Guo J, Lan Z. Effect of transition metal on the hydrogen storage properties of Mg–Al alloy. J Mater Sci 2017;52:2392–9. https://doi.org/10.1007/s10853-016-0533-0.

[61] Tien HY, Tanniru M, Wu CY, Ebrahimi F. Mechanism of hydrogen capacity dependence on the hydrogenation temperature. Scripta Mater 2010;62:274–7. https://doi.org/10.1016/j.scriptamat.2009.11.017.

[62] Crivello JC, Dam B, Denys RV, Dornheim M, Grant DM, Huot J, et al. Review of magnesium hydride-based materials: development and optimisation. Appl Phys Mater Sci Process 2016;122:1–20. https://doi.org/10.1007/s00339-016-9602-0.

[63] Bellosta von Colbe J, Ares JR, Barale J, Baricco M, Buckley C, Capurso G, et al. Application of hydrides in hydrogen storage and compression: achievements, outlook and perspectives. Int J Hydrogen Energy 2019;44:7780–808. https://doi.org/10.1016/j.ijhydene.2019.01.104.

[64] Luo Q, Li J, Li B, Liu B, Shao H, Li Q. Kinetics in Mg-based hydrogen storage materials: enhancement and mechanism. J Magnesium Alloys 2019;7:58–71. https://doi.org/10.1016/j.jma.2018.12.001.

[65] Lu C, Liu H, Xu L, Luo H, He S, Duan X, et al. Two-dimensional vanadium carbide for simultaneously tailoring the hydrogen sorption thermodynamics and kinetics of magnesium hydride. J Magnesium Alloys 2021;10:1051–65. https://doi.org/10.1016/j.jma.2021.03.030.

[66] Luo Q, Li J, Li B, Liu B, Shao H, Li Q. Kinetics in Mg-based hydrogen storage materials: enhancement and mechanism. J Magnesium Alloys 2019;7:58–71. https://doi.org/10.1016/J.JMA.2018.12.001.

[67] Yao P, Jiang Y, Liu Y, Wu C, Chou KC, Lyu T, et al. Catalytic effect of Ni@rGO on the hydrogen storage properties of MgH2. J Magnesium Alloys 2020;8:461–71. https://doi.org/10.1016/j.jma.2019.06.006.

[68] Reier T, Oezaslan M, Strasser P. Electrocatalytic oxygen evolution reaction (OER) on Ru, Ir, and pt catalysts: a comparative study of nanoparticles and bulk materials. ACS Catal 2012;2:1765–72. https://doi.org/10.1021/cs3003098.